

# Study of the IC 443 region with the HAWC observatory

R. Alfaro<sup>1</sup>, C. Alvarez<sup>2</sup>, M. Araya<sup>3</sup>, J.C. Arteaga-Velázquez<sup>4</sup>, D. Avila Rojas<sup>5</sup>, H.A. Ayala Solares<sup>6</sup>, R. Babu<sup>7</sup>, A. Bernal<sup>5</sup>, K.S. Caballero-Mora<sup>2</sup>, T. Capistran<sup>8</sup>, A. Carramiñana<sup>9</sup>, S. Casanova<sup>10</sup>, U. Cotti<sup>4</sup>, J. Cotzomi<sup>11</sup>, S. Coutiño de León<sup>12</sup>, E. De la Fuente<sup>13</sup>, D. Depaoli<sup>14</sup>, P. Desiati<sup>15</sup>, N. Di Lalla<sup>16</sup>, R. Diaz Hernandez<sup>9</sup>, B.L. Dingus<sup>17</sup>, M.A. DuVernois<sup>15</sup>, J.C. Díaz-Vélez<sup>15</sup>, T. Ergin<sup>7</sup>, C. Espinoza<sup>1</sup>, K. Fang<sup>15</sup>, N. Fraija<sup>5</sup>, S. Fraija<sup>5</sup>, J.A. García-González<sup>18</sup>, H. Goksu<sup>14</sup>, J.A. González-Cervera<sup>4</sup>, M.M. González<sup>5</sup>, J.A. Goodman<sup>19</sup>, S. Groetsch<sup>26</sup>, J.P. Harding<sup>17</sup>, S. Hernández-Cadena<sup>32</sup>, I. Herzog<sup>7</sup>, J. Hinton<sup>14</sup>, D. Huang<sup>19</sup>, F. Hueyotl-Zahuantitla<sup>2</sup>, P. Hüntemeyer<sup>26</sup>, S. Kaufmann<sup>20</sup>, A. Lara<sup>21</sup>, J. Lee<sup>22</sup>, H. León Vargas<sup>1</sup>, J.T. Linnemann<sup>7</sup>, A.L. Longinotti<sup>5</sup>, G. Luis-Raya<sup>20</sup>, K. Malone<sup>17</sup>, O. Martínez<sup>11</sup>, J. Martínez-Castro<sup>24</sup>, J.A. Matthews<sup>25</sup>, P. Miranda-Romagnoli<sup>27</sup>, J.A. Montes<sup>5</sup>, J.A. Morales-Soto<sup>4</sup>, E. Moreno<sup>11</sup>, M. Mostafá<sup>23</sup>, M. Najafi<sup>26</sup>, L. Nellen<sup>28</sup>, M.U. Nisa<sup>7</sup>, R. Noriega-Papaqui<sup>27</sup>, L. Olivera-Nieto<sup>14</sup>, N. Omodei<sup>16</sup>, M. Osorio<sup>5</sup>, E. Ponce<sup>11</sup>, Y. Pérez Araujo<sup>1</sup>, E.G. Pérez-Pérez<sup>20</sup>, C.D. Rho<sup>29</sup>, D. Rosa-González<sup>9</sup>, M. Roth<sup>17</sup>, E. Ruiz-Velasco<sup>30</sup>, H. Salazar<sup>11</sup>, A. Sandoval<sup>1</sup>, M. Schneider<sup>19</sup>, G. Schwefer<sup>14</sup>, J. Serna-Franco<sup>1</sup>, A.J. Smith<sup>19</sup>, Y. Son<sup>22</sup>, R.W. Springer<sup>31</sup>, O. Tibolla<sup>20</sup>, K. Tollefson<sup>7</sup>, I. Torres<sup>9</sup>, R. Torres-Escobedo<sup>32</sup>, R. Turner<sup>26</sup>, X. Wang<sup>26</sup>, Z. Wang<sup>19</sup>, I.J. Watson<sup>22</sup>, H. Wu<sup>15</sup>, S. Yu<sup>6</sup>, S. Yun-Cárcamo<sup>19</sup>, H. Zhou<sup>32</sup>, and C. de León<sup>4</sup>

(Affiliations can be found after the references)

Received —; accepted —

## ABSTRACT

**Context.** Supernova remnants are one potential source class considered a PeVatron (i.e. capable of accelerating cosmic rays above PeV energies). The shock fronts produced after the explosion of the supernova are ideal regions for particle acceleration. IC 443 is a supernova remnant that has been studied extensively at different wavelengths. We study this region using very-high-energy gamma-ray data.

**Aims.** We explore the region of IC 443 using 2966 days of gamma-ray data from the HAWC observatory. We study the emission of this supernova remnant and search for signatures that would show acceleration of (hadronic) cosmic rays at the PeV range.

**Methods.** We use the maximum likelihood estimation and a likelihood ratio test to perform a multi-source fitting search. We find the best-fit morphology and spectrum of the IC 443 region above  $\sim 300$  GeV that best describes the HAWC data.

**Results.** We observe a point source located at ( $\alpha=94.42^\circ$ ,  $\delta=22.35^\circ$ ) that we associate with IC 443. The measured spectrum is a simple power law with an index of  $-3.14 \pm 0.18$ , which is consistent with previous TeV observations. We also find a new extended component in the region whose emission is described by a simple power law with an index of  $-2.49 \pm 0.08$  and which we call HAWC J0615+2213.

**Conclusions.** Although we cannot confirm that IC 443 is a hadronic PeVatron, we do not find any sign that the spectrum has a cut off at tens of TeV energies, with the spectrum extending to  $\sim 30$  TeV. Furthermore, we find a new extended source in the region. While we show evidence that this new source might be a new TeV halo, we defer a detailed analysis of this new source to another publication.

**Key words.** gamma rays – SNR – TeV Halos

## 1. Introduction: The IC 443 Region

A supernova explosion occurs when the gravitational force of a star overcomes the internal pressure supporting it against collapse. This loss of pressure happens when a massive star exhausts its thermonuclear fuel. Alternatively, a gravitational collapse may happen when a white dwarf accretes enough mass from a companion star, surpassing its internal pressure. The aftermath of this explosion produces a supernova remnant, composed of ejected material expanding outward and bounded by a shock wave, along with the shocked gas that once surrounded the star. Supernova remnants are considered one of the primary sources of galactic cosmic rays and are one of the candidates to be PeVatrons—astrophysical sources capable of accelerating cosmic rays up to PeV energies—depending on the type of the supernova (Cristofari et al. 2020; Vink 2022).

IC 443—the Jellyfish Nebula—is a supernova remnant discovered by the German-American astronomer Max Wolf in 1892 (Wolf 1893). The position of IC 443, as it appears in the Green Catalog of Supernova Remnants (Green 2019), is at ( $\alpha=94.25^\circ$ ,  $\delta=22.56^\circ$ ) in celestial coordinates (J2000). This remnant has been studied in detail across the entire electromagnetic spectrum.

Radio observations have mapped the cold gas and dust structures within the supernova remnant. The radio emissions indicate regions of synchrotron radiation, where relativistic electrons spiral around magnetic fields, and provide information about the magnetic environment of the remnant (Erickson & Mahoney 1985; Castelletti et al. 2011; Lee et al. 2008). Optical observations have helped delineate the boundaries of the supernova remnant and identify regions of high-energy interactions between the surrounding interstellar medium and the shock waves (Fesen 1984). Infrared observations highlight the presence of warm dust and molecular

gas within the supernova remnant. They also reveal regions where shock waves from the explosion heat the surrounding material and show the distribution of cold, dense molecular clouds interacting with the expanding shock fronts (Li et al. 2022). X-ray observations of IC 443, such as those by Gaensler et al. (2006); Zhang et al. (2018), and Troja et al. (2006), reveal the hot, high-energy gas created by the shock waves of the supernova explosion. Furthermore, these observations have helped identify the progenitor of IC 443 as the neutron star CXOU J061705.3+222127 (Olbert et al. 2001). They have also provided evidence that IC 443 was a Type II supernova (Troja et al. 2008). High-energy observations of this supernova remnant were performed by VERITAS (Acciari et al. 2009), MAGIC (Albert et al. 2007), and Fermi-LAT (Abdo et al. 2010). Gamma-ray emission in the Fermi energy band was confirmed to be the result from the interaction of hadronic cosmic rays accelerated in the SNR with molecular clouds surrounding the remnant after observing the pionic bump in the spectral energy distribution (Ackermann et al. 2013).

Other studies have shown the complexity in this region, with the supernova remnant G189.6+03.3 overlapping with IC 443 and possibly interacting with it (Camilloni & Becker 2023). These studies suggest that they are at the same distance, with distances between 1.5 kpc to 2.5 kpc (Ambrocio-Cruz et al. 2017). Their ages are uncertain, ranging from a minimum of 3 kyr and a maximum of about 30 kyr (Camilloni & Becker 2023). Ustamujic et al. (2021) measured an age of  $\sim 8$  kyr after comparing a hydrodynamic model for IC 443 describing the interaction of the remnant with the environment and comparing the expected X-ray emission with XMM-Newton data.

In this work, we report our observations of this region using HAWC data. Unexpectedly, we have also found a new gamma-ray component with an extended morphology and a hard spectral flux. We investigate two hypotheses to explain this emission: (1) secondary gamma rays from cosmic rays interacting with gas in the region; (2) a new TeV halo produced by the pulsar B0611+22. This pulsar was discovered by Davies, J. and Lyne, A. and Seiradakis, J. (1972). It is  $\sim 90$  kyr old and is located at 3.55 kpc (Deller et al. 2019)<sup>1</sup>. Most recent observations on these pulsar have been in radio and X-rays, with the latter only showing upper limits (Rajwade et al. 2016).

## 2. The HAWC Observatory and the Dataset

The High Altitude Water Cherenkov (HAWC) Observatory is a gamma-ray detector located at 4100 m a.s.l. in central Mexico, near the Pico de Orizaba volcano. The detector consists of 300 steel tanks containing 180,000 litres of water, which serves as the refractive medium used to produce Cherenkov light. This light is detected by four photomultipliers (PMTs), three of which are eight inches and one being ten inches in size. The PMTs are anchored at the bottom of the tanks and facing upwards. When a gamma-ray interacts with the atmosphere, it produces a cascade of particles, known as an extensive air shower. The secondary particles propagate and spread out through the atmosphere, expanding the shower front up to a point where the energy is no longer sufficient. The particles in the shower front penetrate the steel tanks and produce Cherenkov light in the water that the PMTs detect. The detector is sensitive to gamma rays with energies between 300 GeV to  $>100$  TeV. It has a high-duty cycle of about  $>95\%$  and an instantaneous field of view of 2 sr, covering  $2/3$  of the sky every day (Abeysekara et al. 2017; Albert et al. 2020; Abeysekara et al. 2023).

We recover the information of the primary gamma ray—its location in the sky and energy—by using the triggered time and the measured charge in each PMT. The energy of the gamma ray is reconstructed with two independent methods. One is by fitting the shower profile after locating the core of the shower in the array. The other is a neural network to estimate the energy of the gamma ray. Both methods are described in Albert et al. (2024).

For the analysis, we have used two binning schemes. The first binning scheme is based on the ratio of triggered to active PMTs during a shower event. We denote this ratio as  $f_{\text{hit}}$ . In this scheme, we consider events whose reconstructed cores are measured inside and outside the main array. For the second binning scheme, along with the  $f_{\text{hit}}$  information, we also bin the events according to their reconstructed energy, creating what we refer to as energy scheme. This second scheme only considers events with reconstructed cores inside the main array. We use both schemes for our analysis. The first scheme gives us more statistics and we use it to find the best-fit morphology of the sources in the region. The second scheme is better suited to obtain spectral points since we have more accurate energy information. All the schemes give a similar flux measurement as seen in Figure 9 of the HAWC performance paper (Albert et al. 2024).

## 3. Analysis and Results

### 3.1. Analysis Method

We use data collected from 2015 to 2023. The livetime is 2966 days using the  $f_{\text{hit}}$  bin scheme, while with the reconstructed energy scheme, it is 2769 days since we remove data from the time period where HAWC was under construction and not all tanks were operational.

We apply a gamma-hadron selection cut found in Albert et al. (2024), and estimate the background using the method described in section 4.3 of (Abeysekara et al. 2019). Once we have the estimated background, we proceed with the analysis, based on the maximum likelihood estimation method. For the analysis we use the Multi-Mission Maximum Likelihood (threeML) framework with the HAWC Accelerated Likelihood (HAL plugin) as described in Vianello et al. (2015); Abeysekara et al. (2022). ThreeML uses the likelihood ratio test to determine whether one model is better than another. The test statistic is defined as

$$TS = 2(\ln L_i - \ln L_j), \quad (1)$$

<sup>1</sup> The pulsar has a dispersion measure of  $96.91 \text{ pc cm}^{-3}$ , which puts the pulsar at 1.74 kpc or 3.5 kpc, depending on the model used to measure the distance (see Yao et al. 2017). However, Deller et al. (2019) have parallax measurements and hence we decided to use this value.

where  $L_{i,j}$  are the maximum likelihoods of models  $i, j$ . It is important to remark that we also use this statistic when generating sky maps, where the calculation is performed for each individual pixel.

The algorithm we use to determine the morphology of the region is described in Albert et al. (2023), with the difference that we now use the High-Energy Radiative Messengers (HERMES) diffuse emission template as the galactic diffuse emission (GDE) model (Dundovic et al. 2021). HERMES is a spatial propagation template based on the DRAGON cosmic-ray propagation code (Evoli et al. 2017). The model includes pionic gamma rays, produced by the interaction of the sea of cosmic rays with neutral and molecular hydrogen. It also includes inverse Compton from the cosmic-ray leptons scattering on low-energy photons in the Galaxy such as UV, optical, infrared or microwave photons. This new GDE model has the advantage that it considers the morphology of the gas in the region, whereas Albert et al. (2023) used a Gaussian shape as a function of galactic latitude. When fitting the GDE model, we free a unit-less factor parameter that scales the normalization of the baseline diffuse flux calculated by HERMES.

To summarize the algorithm used in Albert et al. (2023), we first search for all possible point sources in the region and assume a simple power-law spectrum for each one as shown in Algorithm 1. Then, each point source is tested as an extended source as described in Algorithm 2. Once we have found the final morphology of each source, we test for curvature in the spectrum, with the process described in Algorithm 3.

---

#### Algorithm 1 Point Source Morphology Search

---

- 1: Fit scale parameter of the GDE model
- 2: **while** TS > 25 **do**
- 3:     Add point source with a simple power-law spectrum at the hotspot with maximum significance in the skymap.

$$\Phi_{SPL} = \Phi_0 \left( \frac{E}{E_{\text{piv}}} \right)^\alpha [\text{TeV}^{-1} \text{cm}^{-2} \text{s}^{-1}], \quad (2)$$

where  $\Phi_0$  is the normalization at the pivot energy  $E_{\text{piv}}$ , and  $\alpha$  is the spectral index.

- 4:     Calculate TS between model with extra point source and previous accepted model.
  - 5:     Keep new model and return to step 2.
  - 6: **end while**
  - 7: Move to extended source morphology search.
- 

---

#### Algorithm 2 Extended Source Morphology Search

---

- 1: Replace the point source with the highest TS with a Gaussian morphology (see appendix for the formula) and leave all other sources as point sources. Locations stay fixed. Fit the spectra and extension.
  - 2: Check TS between previous model and new model
  - 3: **if** TS > 16 **then**
  - 4:     Accept the new model
  - 5: **else**
  - 6:     Reject the extended source model and move to the next highest TS value source. Go to step 1.
  - 7: **end if**
  - 8: Check TS of point sources in the accepted model
  - 9: **if** TS > 16 of all the point sources **then**
  - 10:     Go to Step 1.
  - 11: **else if** TS < 16 of any point source **then**
  - 12:     Remove the source(s) and refit the new model while floating all parameters. Go to Step 8 if there are point sources remaining, otherwise end the study if no more point sources remain for extension testing.
  - 13: **end if**
- 

The final step is to check whether the spectrum of the sources has a cutoff or curvature. We have tested for a logarithmic parabola and a power law with exponential cutoff, whose functional forms are:

$$\Phi = \Phi_{SPL} \left( \frac{E}{E_{\text{piv}}} \right)^{\beta \ln(E/E_{\text{piv}})}, \quad (3)$$

where  $\Phi_{SPL}$  is the same as in Equation 2 and  $\beta$  is the curvature parameter;

$$\Phi = \Phi_{SPL} \exp\left(-\frac{E}{E_{\text{cutoff}}}\right), \quad (4)$$

where  $\Phi_{SPL}$  is the same as in Equation 2 and  $E_{\text{cutoff}}$  is the cutoff energy.

### 3.2. Observations

Figure 1 shows the HAWC  $f_{\text{hit}}$  significance map of the region of IC443. The bright region shows the region of interest used for the analysis. The best-fit model describing the region together with the GDE model is a point source (PS) and an extended source

---

**Algorithm 3** Spectrum Test

---

- 1: Fix position of sources.
  - 2: Calculate the log-likelihood of the model with all sources having a simple powerlaw
  - 3: Select source with highest TS.
  - 4: Change its spectrum from simple power law to a model with curvature. Fit the new model
  - 5: **while** TS > 16 between new model and old model **do**
  - 6:     Keep the new model. Move back to step 3.
  - 7: **end while**
- 

(ES). We found no significant preference for a spectral curvature for either source. We associate the point source with IC 443. For the extended source, which we name HAWC J0615+2213, we did not find a possible counterpart in the literature. Therefore, we investigate two possibilities: emission originating from the interaction of freshly injected cosmic rays with the interstellar medium, or a new TeV Halo object. We defer this discussion to Sect. 4.

The position of the point source is located  $0.26^\circ$  away from the Green catalog position of IC 443 and  $0.14^\circ$  from the pulsar wind nebula associated with the neutron star CXOU J061705.3+222212. The centroid of the extended source is  $0.63^\circ$  from IC 443,  $0.57^\circ$  from CXOU J061705.3+222212, and  $0.29^\circ$  from the pulsar B0611+22. We observe no significant excess in the direction of the supernova remnant G189.6+03.3. The source parameter results are summarized in Table 1. The pivot energy,  $E_{\text{piv}}$ , that reduces the correlation between the parameters was found to be 2.3 TeV. Table 2 shows the comparison of the fitted spectral parameters between the  $f_{\text{hit}}$  binning scheme and the energy binning scheme.

Figure 2 shows the map of the best-fit model, as well as the residual map of the region, and the significance distribution of the sky. The significance distribution is relatively close to a Gaussian distribution, showing that the model adequately describes most of the signal and the remaining is only background. Figure 3 shows each source after subtracting either the extended source or the point source from the original map.

**Table 1.** Results of the analysis in the region of IC 443 using the  $f_{\text{hit}}$  scheme.

Source	$\Phi_0$ [ $\text{TeV}^{-1}\text{cm}^{-2}\text{s}^{-1}$ ]	Index	R.A. [deg]	Decl. [deg]	$\sigma$ [deg]
PS	$(5.9 \pm 1.3^{+0.21}_{-0.86}) \times 10^{-14}$	$-3.14 \pm 0.18^{+0.08}_{-0.09}$	$94.42^{+0.07+0.009}_{-0.05-0.008}$	$22.35^{+0.06+0.035}_{-0.07-0.003}$	–
ES	$(3.18^{+1.37+0.19}_{-0.92-0.37}) \times 10^{-13}$	$-2.49 \pm 0.08^{+0.009}_{-0.028}$	$93.67 \pm 0.19^{+0.016}_{-0.004}$	$22.22 \pm 0.20^{+0.015}_{-0.007}$	$1.05^{+0.21+0.004}_{-0.18-0.013}$
GDE model	$2.62 \pm 1.20^{+0.07*}_{-0.30}$	–	–	–	–

**Notes.** First set of uncertainties are statistical while the second set are systematic. The normalization of the two sources is at  $E_{\text{piv}} = 2.3$  TeV. PS is associated with IC 443. ES is the new source HAWC J0615+2213.

**Notes.** \*Scale factor. Unitless

**Table 2.** Comparison of the spectral parameters results between each binning scheme.

Parameter	$f_{\text{hit}}$ Scheme	Energy Scheme
PS $\Phi_0$	$(5.9 \pm 1.3) \times 10^{-14}$	$(7.8^{+1.5}_{-1.3}) \times 10^{-14}$
PS Index	$-3.14 \pm 0.18$	$-3.07 \pm 0.12$
ES $\Phi_0$	$(3.18^{+1.37}_{-0.92}) \times 10^{-13}$	$(3.0^{+0.8}_{-0.6}) \times 10^{-13}$
ES Index	$-2.49 \pm 0.08$	$-2.61 \pm 0.09$

**Notes.** Comparison between the two analysis bin schemes. Uncertainties are statistical only. Units of K are in [ $\text{TeV}^{-1}\text{cm}^{-2}\text{s}^{-1}$ ].

The energy ranges in which the sources are significantly detected are calculated using the method described in Abeysekara et al. (2017). At the  $1\sigma$ , or 68% confidence level, these are [0.3,30] TeV for the point source and [0.7,47] TeV for the extended source.

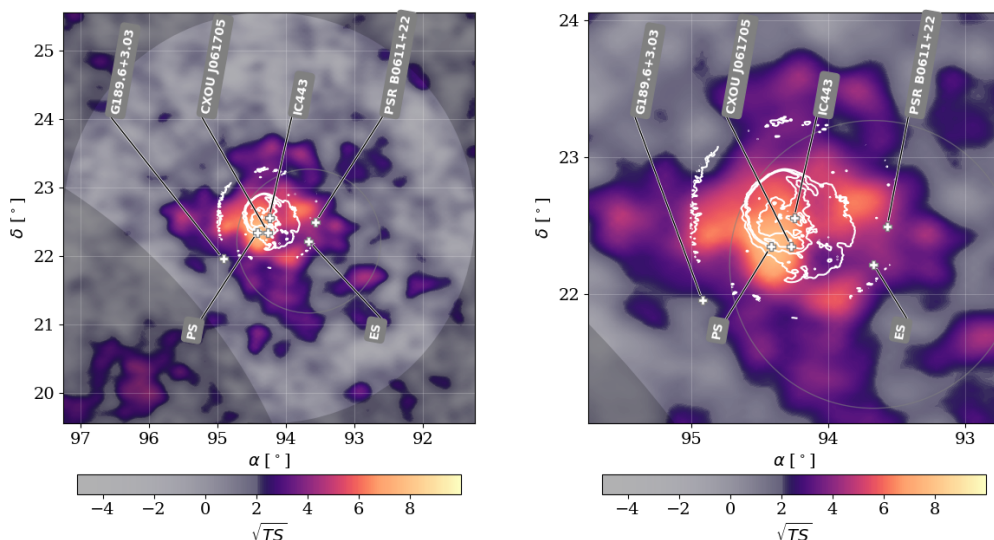


**Fig. 1.** IC 443 region seen by HAWC using the  $f_{\text{hit}}$  analysis bins. The map assumes a point source morphology with an index of  $-3.14$ . The radio contours (in white) are from Lee et al. (2008). The region of interest used for the analysis is also shown with the change of brightness in the sky map. The positions of IC 443 and G189.6+3.03 are from the Green Catalog Green (2019). Position of CXOU J061705+222127 is from Olbert et al. (2001). Position of the pulsar B0611+22 comes from Davies, J. and Lyne, A. and Seiradakis, J. (1972). The positions found in the analysis for the point source (PS) and extended source (ES) are also shown. Gray circle is the width of the ES.

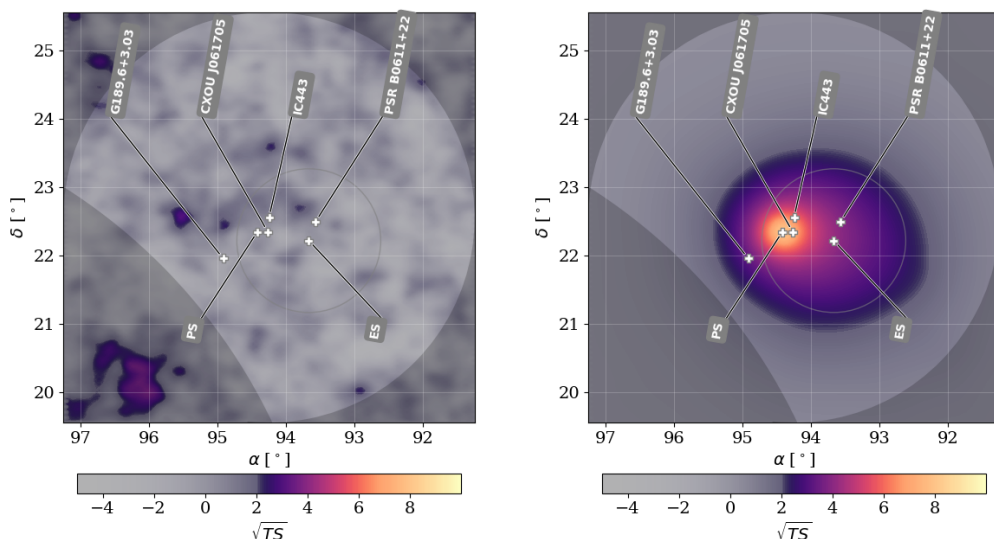


**Fig. 2.** Top left: Residual sky map after fitting the best-fit model using the  $f_{\text{hit}}$  analysis bins. The region of interest used for the analysis is also shown with the change of brightness in the skymap. Top right: Best-fit sky map model. No significant excesses are observed after subtracting the best-fit model.

### 3.2.1. Systematics

To account for detector biases, we performed the analysis with multiple detector responses that consider different calibration, detector and simulation effects. This includes calibration performance, charge uncertainty, PMT efficiency and PMT threshold. We also estimated a systematic based on the modeling of the region by setting the scaling factor of the GDE model to one. We find the difference between the default and systematic results and add them in quadrature to determine the final systematic uncertainties (see Abeyssekara et al. 2017; Albert et al. 2020, for more information). The uncertainties are listed in Table 1.

### 3.3. Spectral Energy Distributions (SED)

As mentioned before, the 1D binning scheme is used to obtain the best spectral shape of a source with threeML. To obtain the spectral points, we use the 2D binning scheme. We fix all the parameters of the model except for the normalization of the source in each energy bin. Tables 3 and 4 present the differential particle flux measured by HAWC and the  $E^2$ -weighted differential particle

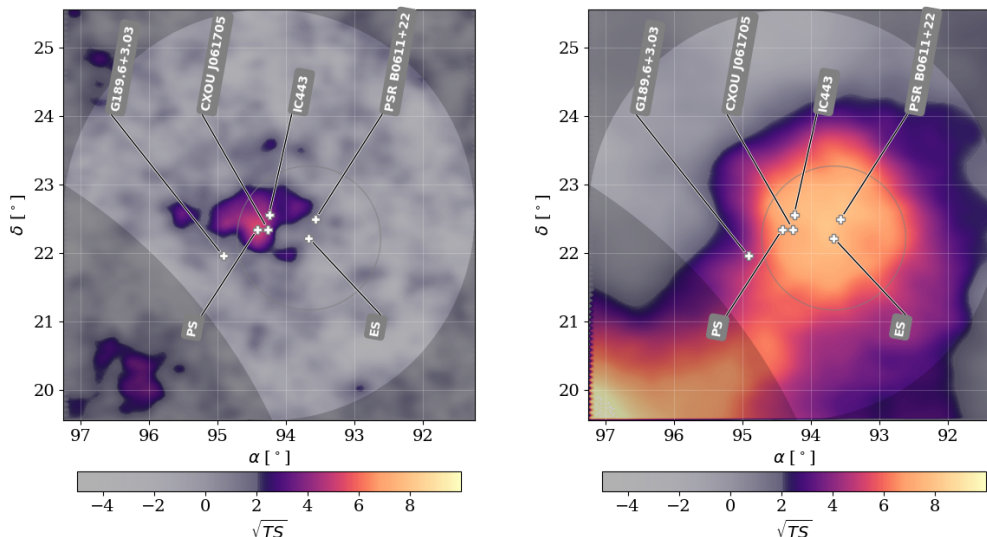


**Fig. 3.** Residual maps of the region for the  $f_{\text{hit}}$  analysis bins. Left: subtracting the extended source. Right: subtracting the point source. In the second significance map, we made it assuming an extension of  $1.05^\circ$ . On the lower left of the plot the Geminga Halo is visible. The region of interest used for the analysis is shown with the change of brightness in the sky map.

flux is shown in Fig. 4. The figure also compares the spectral model fitted with the  $f_{\text{hit}}$  scheme and the energy bin scheme, showing that they are consistent with each other.

**Table 3.** SED flux points of the PS IC 443

Energy [TeV]	Flux [ $\text{TeV}^{-1}\text{cm}^{-2}\text{s}^{-1}$ ]	TS
0.3	$(3.3^{+1.6}_{-1.1}) \times 10^{-11}$	6.2
1.3	$(5.0^{+1.3}_{-1.0}) \times 10^{-13}$	18.5
4.7	$(6.2^{+3.3}_{-2.1}) \times 10^{-15}$	5.4
15.4	$(3.3^{+1.4}_{-1.0}) \times 10^{-16}$	11.1
38.2	$< 4.5 \times 10^{-17}$	0.3

**Notes.** Uncertainties are statistical only. U.L. is 90% C.L.

**Table 4.** SED flux points of the ES HAWC J0615+2213

Energy [TeV]	Flux [ $\text{TeV}^{-1}\text{cm}^{-2}\text{s}^{-1}$ ]	TS
0.5	$< 3.8 \times 10^{-11}$	0.5
1.6	$(5.8^{+3.8}_{-2.3}) \times 10^{-13}$	3.8
5.6	$(3.5^{+1.5}_{-1.0}) \times 10^{-14}$	8.4
17.6	$(3.1^{+0.8}_{-0.6}) \times 10^{-15}$	23.1
39.8	$(1.4^{+1.0}_{-0.6}) \times 10^{-16}$	3.2

**Notes.** Uncertainties are statistical only. U.L. is 90% C.L.

## 4. Discussion

### 4.1. Multi-wavelength observations of IC 443

Several researchers have performed extensive multi-wavelength studies of IC 443 over the years. Early works by Chevalier (1999) and Baring et al. (1999) laid the groundwork of multi-wavelength observations, focusing mainly on the radio and X-ray components; while more recent studies as Ackermann et al. (2013); Zhang et al. (2018) and Sharma et al. (2023), have furthered our understanding at higher energies up to 1 TeV. We use the new HAWC observations to extend the multi-wavelength analysis up to 30 TeV. As mentioned earlier, we associate the point source we found in Sect. 3 with IC 443.

In the very-high-energy ( $>100$  MeV) part of the electromagnetic spectrum, Ackermann et al. (2013) demonstrated that gamma-ray emission is primarily due to the decay of neutral pions produced in inelastic collisions between cosmic-ray protons and dense molecular clouds in the region (Seta et al. 1998; Ustamujic et al. 2021). They also explored leptonic models, showing that these models could not account for the observed gamma-ray flux due to energetic constraints (see Abdo et al. 2009). These constraints arise from the maximum energy that electrons can achieve in an environment like IC 443. Electron acceleration is restricted by the underlying mechanism, such as diffusive shock acceleration (DSA), and by substantial energy losses due to synchrotron radiation,

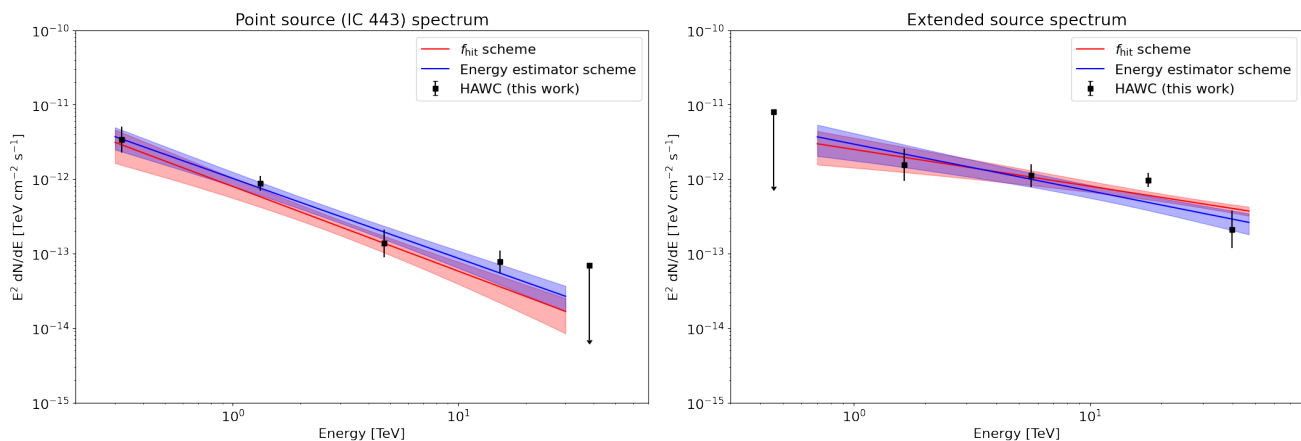


**Fig. 4.** Spectrum of the two sources seen by HAWC. Left is the spectrum of the point source, which we associate with IC 443. Right is the spectrum of the extended source.

inverse Compton scattering, and bremsstrahlung. These losses are further amplified by the dense molecular cloud surrounding IC 443.

Under typical magnetic fields ( $\sim 100 \mu\text{G}$ ) and accounting for both synchrotron and inverse Compton losses, the maximum energy an electron can gain is approximately 5 TeV (Petrosian 2012; Yamaguchi et al. 2009). When bremsstrahlung losses are included in regions with higher gas densities (up to  $100 \text{ cm}^{-3}$ ) (Troja et al. 2008), this maximum decreases further to around 3 TeV. Even with non-linear shock effects that amplify the magnetic field up to  $300 \mu\text{G}$ , the maximum achievable electron energy is only  $\sim 10$  TeV. Thus, while electrons can contribute to high-energy emission, they cannot explain gamma rays up to 30 TeV. This limitation makes hadronic processes a more plausible explanation for IC 443's observed gamma-ray spectrum (Guo et al. 2014; Zhang & Yan 2011).

Protons can achieve significantly higher energies due to their relatively low energy losses. The maximum energy for protons, achievable via DSA, depends on factors such as shock speed, magnetic field strength, and remnant size. For IC 443, typical values include a shock speed of  $300 \text{ km s}^{-1}$  (Lee et al. 2008; Troja et al. 2008), a magnetic field strength of  $10 \mu\text{G}$  (Yamaguchi et al. 2009), and a remnant size of 10.9 pc (Troja et al. 2008). These parameters suggest that protons could theoretically reach energies up to  $\sim 65$  TeV (Drury 1983; Lagage & Cesarsky 1983; Bell et al. 2013). With the inclusion of non-linear diffusive shock acceleration (NLDSA) effects, which amplify the magnetic field, this maximum energy may extend to 100 TeV or even higher, potentially approaching 1 PeV (Bell 2004; Bell et al. 2013; Caprioli et al. 2009).

To test these estimates of the maximum proton energies, we perform an analysis using the Markov Chain Monte Carlo (MCMC) software *Naima* (Zabalza 2015). This software fits data to non-thermal emission models by optimizing the parameters of the parent particle spectra. Additionally, it calculates the Bayesian Information Criterion (BIC) for the models, which we use to compare and evaluate their performance.

We incorporate observations from Fermi (Abdo et al. 2010), VERITAS (Acciari et al. 2009), MAGIC (Albert et al. 2007), and the results presented here. Additionally, the recently commissioned LHAASO detector—a gamma-ray observatory with better sensitivity above 10 TeV compared to HAWC—has reported extended emission in the region as part of its catalog search. LHAASO observes a source with a width of  $(0.59 \pm 0.08)^\circ$  located at coordinates  $94.35^\circ, 22.57^\circ$ . Their analysis using LHAASO-WCDA data, based on a simple power-law model, yielded a differential particle flux at 3 TeV of  $(1.95 \pm 0.27) \times 10^{-13} \text{ TeV}^{-1} \text{ cm}^{-2} \text{ s}^{-1}$  with a spectral index of  $-2.92 \pm 0.14$  in the energy range between 1 TeV to 25 TeV. An upper limit of  $0.17 \times 10^{-15} \text{ TeV}^{-1} \text{ cm}^{-2} \text{ s}^{-1}$  at 50 TeV was set using LHAASO-KM2A (Cao et al. 2024). However, further detailed analysis is required to determine whether this observation aligns with the morphology identified in our study. Therefore, we do not include the LHAASO data in our fitting (See appendix B where we test the LHAASO model with HAWC data). Based on the arguments outlined above, we use a pion decay model to explain the gamma-ray emission, similar to the approach in Ackermann et al. (2013). We set the maximum energy values to 65 TeV and 1 PeV for the proton distribution for the test. The proton spectrum is modeled with both a broken power law and a power law with an exponential cutoff:

$$f(E) = \begin{cases} A(E/E_0)^{-\alpha_1} & E < E_{\text{break}} \\ A(E_{\text{break}}/E_0)^{\alpha_2 - \alpha_1} (E/E_0)^{-\alpha_2} & E \geq E_{\text{break}} \end{cases} \quad (5)$$

$$f(E) = A(E/E_0)^{-\alpha} \exp(-E/E_{\text{cutoff}}), \quad (6)$$

where  $A$  is the normalization of the spectrum at energy  $E_0$ ;  $\alpha_1$  and  $\alpha_2$  are the spectral indices before and after the break energy  $E_{\text{break}}$ , while  $\alpha$  is the spectral index in the exponential cutoff model;  $E_{\text{cutoff}}$  is the cutoff energy. The fitted parameters results after running the aforementioned models are shown in Table 5.

The results are consistent when we compare between the different maximum energies in each of the cosmic-ray distributions. When comparing between spectral models, the broken power-law model provides a better fit than the exponential cutoff based on the BIC. We also fitted the density of the environment, which is in the same order of magnitude as shown in Ustamujic et al. (2021) and can impact the total energy of the protons required to produce gamma rays. These models yield a total proton energy content



**Table 5.** Parameter results of the Naima modeling. We tested two spectral functions for the cosmic-ray spectrum and two maximum proton energies.

	Broken power law		Exponential cutoff	
	65 TeV	1 PeV	65 TeV	1 PeV
$\log(A [\text{TeV}^{-1}])$	$47.4 \pm 0.1$	$47.3 \pm 0.1$	$49.3 \pm 0.1$	$49.4 \pm 0.1$
$\alpha_1$	$2.27 \pm 0.04$	$2.28 \pm 0.04$	$2.35 \pm 0.3$	$2.34 \pm 0.03$
$\alpha_2$	$3.03 \pm 0.06$	$3.03 \pm 0.05$	—	—
$E_{\text{break/cutoff}} [\text{TeV}]$	$0.10 \pm 0.4$	$0.10 \pm 0.03$	$1.3^{+0.3}_{-0.2}$	$1.2^{+0.3}_{-0.2}$
$n [\text{cm}^{-3}]$	$204^{+45}_{-36}$	$252^{+68}_{-57}$	$332^{+110}_{-91}$	$290^{+102}_{-70}$
BIC	65.1	65.2	111.2	111.2

**Notes.** Uncertainties are statistical only.

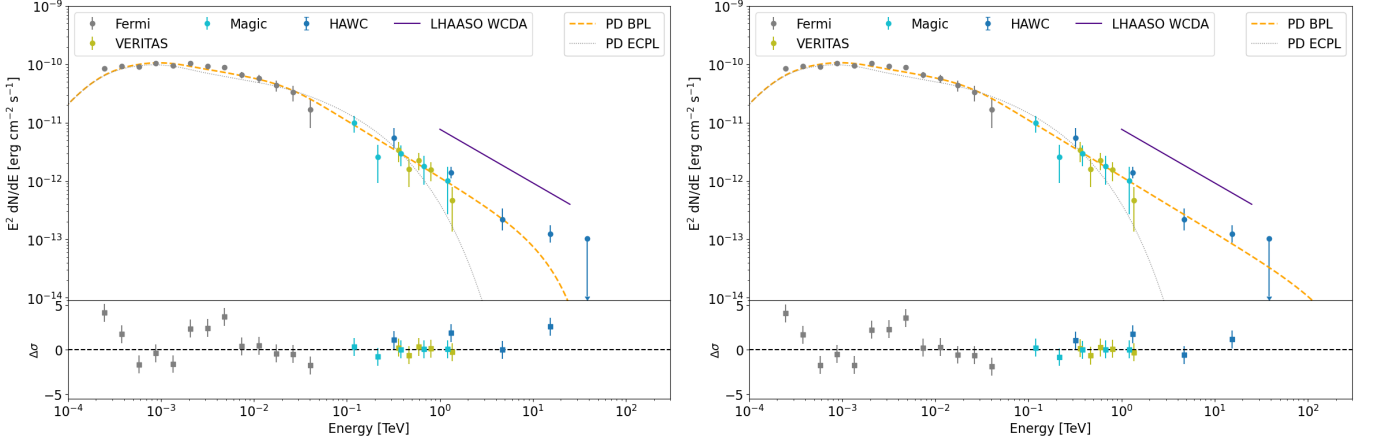


**Fig. 5.** Spectrum of IC 443 in gamma rays. The model is a pion decay with a parent proton spectrum following a broken power law (BPL) or exponential cutoff spectrum (ECPL). On the left, the maximum energy of the protons is 65 TeV, on the right it is 1 PeV. These values are based on theory approximations as mentioned in the main text. In both cases the ECPL does not describe the data above 10 TeV. The model with a higher maximum proton energy provides a better fit to the tail of the spectral distribution.

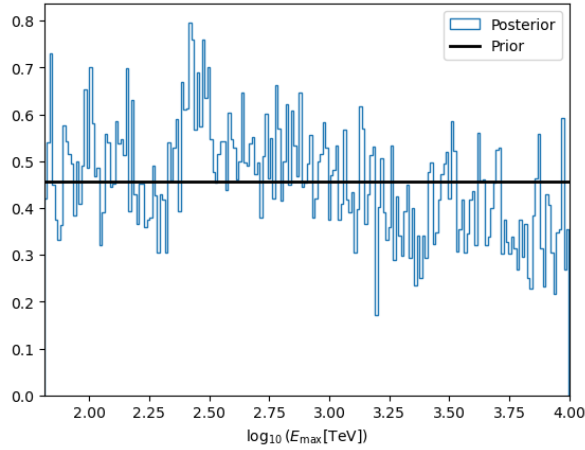


**Fig. 6.** Prior and Posterior distribution of the maximum energy of the proton distribution after fitting a hadronic model with Naima. The distribution is still relatively flat compared to the prior distribution which is a uniform distribution in log space between 65 TeV and 10 PeV.

with  $E \geq 0.8$  GeV of  $W_p \sim [6 - 8] \times 10^{48} (n/200 \text{ cm}^{-3})^{-1}$  erg, which is less than 1 per cent of the total supernova remnant energy of  $\sim 10^{51}$  erg, consistent with Ackermann et al. (2013), even though they assumed a density of  $20 \text{ cm}^{-3}$ . Figure 5 shows that the tail of the distribution is better described by extending the proton spectrum to 1 PeV.

We tested a model where we left the maximum energy of the proton distribution to be free. Since the HAWC data do not show any cutoff, the posterior distribution of the maximum energy remains relatively flat, as it is shown in Fig. 6, compared to a prior uniform distribution in logarithmic space in the range of 65 TeV to 10 PeV.

This suggests that IC 443 has the potential to accelerate cosmic rays to energies beyond the 65 TeV limit predicted by DSA, making it a strong candidate for a PeVatron. Given the constraints on leptonic processes, our findings further support IC 443 as a



compelling source of PeV cosmic rays. However, higher-energy observations are still needed to determine where the gamma-ray spectrum cuts off, as this will provide a direct measure of the maximum energy achievable by protons.

#### 4.2. Origin of the gamma-ray emission from the extended source

The extended emission we found in the analysis is surprising. First, it does not spatially correlate with the other the supernova remnant G189.6, which is  $1.2^\circ$  away from the centroid of the extended source. We see no significant emission from this other remnant, which means that it does not emit gamma rays at a level detectable by HAWC. After discarding this possibility, we investigate two other scenarios next.

##### 4.2.1. Cosmic ray illumination of interstellar gas

The first scenario is illumination of the surrounding interstellar gas by the accelerated cosmic rays from IC 443. Several studies, (e.g. Ustamujic et al. 2021), show that IC 443 is embedded and interacting with the gas clouds surrounding the shell. We want to know if the cosmic rays from the IC 443 can escape and travel further away from the shell.

We start by estimating the power needed to see the gamma-ray emission. Using the observed spectrum of the extended source and assuming that the gas is a few tens of parsecs away from IC 443 and a distance to the region of 1.5 kpc (same as in Ustamujic et al. 2021), we calculate a gamma-ray luminosity of  $\sim 3.17 \times 10^{33}$  erg  $s^{-1}$ . If we assume that the centroid of the extended source is also located at the same distance as IC 443, we can use the width of the 2D Gaussian model to estimate a volume of this region. Assuming also a density of  $1 \text{ cm}^{-3}$ , and using Eq. 2 of Abramowski et al. (2016), we can estimate the energy density of the cosmic rays producing the gamma-ray emission for the extended source above  $E_p = 10E_\gamma = 5 \text{ TeV}$ , giving a value of  $1.53 \text{ eV cm}^{-3}$ . Using the volume again, we can estimate the energy budget of the cosmic rays which is  $\sim 1 \times 10^{49}$  erg, lower than the total energy of the supernova remnant of  $\sim 10^{51}$  erg. However, we still need to determine whether there is target material in this region with which the cosmic rays can interact with.

The gas surveys used in the GDE model are from the Dame (Dame et al. 1987) and the HI4PI (HI4PI Collaboration et al. 2016) surveys. The GDE model considers the sea of cosmic rays interacting with the gas to produce pionic gamma rays and considers the whole gas in the line of sight. With this hypothesis, we test the possibility that IC 443 injects “fresh” cosmic rays into the region as a second component besides the sea of cosmic rays, enhancing the production of pionic gamma rays. Using the kinematic distance tool of Wenger et al. (2018), we estimate a range of velocities, going from 3.5 to  $10 \text{ km s}^{-1}$  corresponding to distances of  $\sim 0.8$  to  $\sim 2.97$  kpc. We do not find enough molecular gas in the region that overlaps with the extended source. However, we find some gas in the atomic hydrogen survey that overlaps spatially with the extended emission. Figure 7 shows the contour lines of the gas column density in the region from the HI4PI survey.

We repeated the analysis with a template model from the gas survey as the new morphology for the extended source (similar to Albert et al. 2021). We assume a simple power-law function for the spectrum. We get a similar result as the 2D Gaussian model, with a normalization of  $(3.88^{+1.5}_{-1.4}) \times 10^{-13} \text{ TeV}^{-1} \text{ cm}^{-2} \text{ s}^{-1}$  and index of  $-2.48^{+0.1}_{-0.5}$ . However, looking at the residual map in Fig. 7, we still see some emission in the region that is not described by this model.

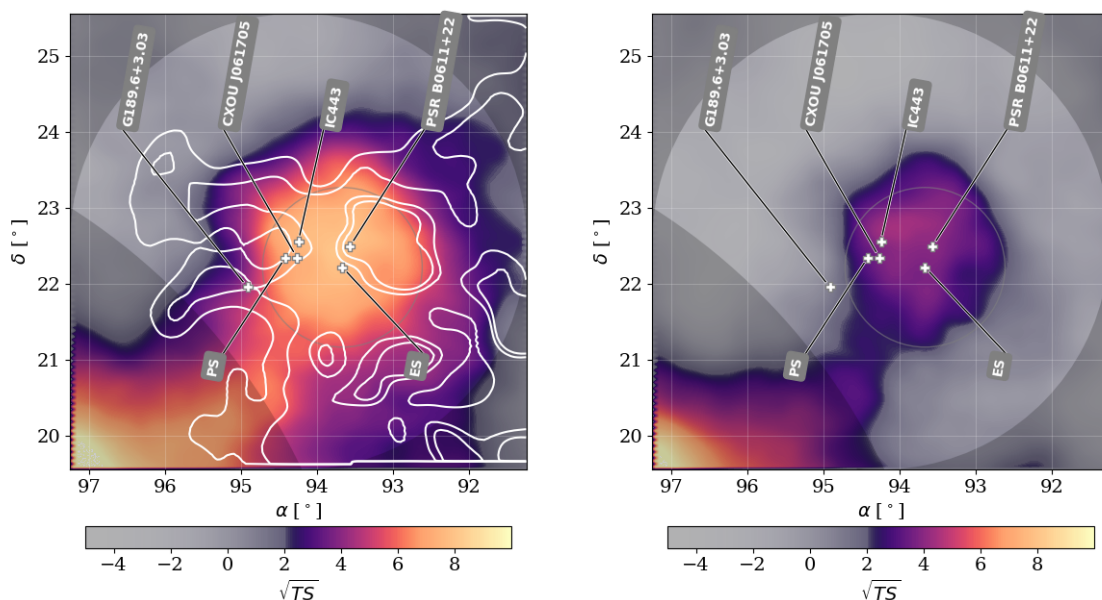


**Fig. 7.** Left: The map is the same as the second map in Fig. 3, but now shows the contour lines of gas in the region from the HI4PI survey. The contour lines correspond to the column density determined after integrating the HI4PI data in the velocity range  $3.5$  to  $10 \text{ km s}^{-1}$ . Right: Residual map of the region after subtracting the model that includes the GDE, the point source and the gas template from the figure on the left. There is still unexplained emission left in the region.

#### 4.2.2. A new TeV Halo

The second hypothesis we investigate for the extended emission is a TeV halo. In Fig. 3, the pulsar B0611+22 is in the middle of the extended source ( $0.29^\circ$  from the best measured position).

Middle-age pulsars ( $\sim 100$  kyr) seem to be the main sources of TeV (or electron) halos. These objects were first described by Linden et al. (2017) as a new type of source, mainly emitting gamma rays through inverse Compton radiation by the accelerated leptons in the PWN. Since then, new models and definitions have been developed for TeV halos. For example, Giacinti et al. (2020) mention that a halo forms after the pulsar and the pulsar wind nebula have escaped the remnant environment, which occurs at a time  $\gtrsim 100$  kyr, close to the age of B0611+22. According to this model, the energy density of the electrons in the region must be lower than the energy density of the interstellar medium, so that inverse Compton losses dominate over synchrotron and bremsstrahlung.

We proceed to calculate some estimates that suggest that this emission is a potentially new TeV Halo.

Using the 2D Gaussian morphology results from Sect. 3, we can estimate the maximum diffusion coefficient in the region. The upper limit for the diffusion coefficient is (Atayan et al. 1995)

$$D \leq \frac{R^2}{4t_e}, \quad (7)$$

where  $t_e$  is the electron cooling time of 12 kyr at 100 TeV by upper-scattering photons from the CMB. Using the gaussian width result,  $\theta = 1.05^\circ$ , we can estimate a radius of this region based on geometry

$$R = d_0 \tan \theta, \quad (8)$$

where  $d_0 = 3.55$  kpc, is the distance to the pulsar.

Using these calculations we get

$$D \leq 2.21 \times 10^{28} \left( \frac{d}{d_0} \right)^2 \left( \frac{t}{t_e} \right)^{-1} \text{ cm}^2 \text{ s}^{-1}. \quad (9)$$

For this emission to be considered a halo, the maximum diffusion coefficient should be smaller than the diffusion coefficient of the ISM, which is  $10^{30} \text{ cm}^2 \text{ s}^{-1}$ . We find that the diffusion coefficient to be  $2.21 \times 10^{28} \text{ cm}^2 \text{ s}^{-1}$ , making this source a possible TeV Halo.

We also estimate the energy density of the electrons,  $\epsilon_e$ , and compare it to that of the interstellar medium. There are a couple of ways to calculate this. We use the pulsar properties to calculate  $\epsilon_e = E_{inj}/V$ , where  $E_{inj} = \dot{E}\tau_c$  is the injected energy, with  $\dot{E}$  as the present spin-down power and  $\tau_c$  as the characteristic age of the pulsar. To determine the volume, we use the radius estimated in Eq. 8. With  $\dot{E} = 6.24 \times 10^{34} \text{ erg s}^{-1}$  and  $\tau_c = 90$  kyr, this estimate gives  $\epsilon_e \approx 0.003 \text{ eV cm}^{-3}$ .

We calculate a second estimate by evaluating the properties of the electron spectrum after fitting an inverse Compton model to the data as it is shown in Fig. 8. Integrating the simple power-law spectrum above 100 GeV yields an energy density of  $0.0016 \text{ eV cm}^{-3}$ , while for the exponential cutoff model, we obtain  $0.0002 \text{ eV cm}^{-3}$ . The parameters used in these models are presented in Appendix C. All estimates are below  $\sim 0.1 \text{ cm}^{-3}$ , the energy density of the interstellar medium. This provides some evidence that the newly observed emission may be associated with a TeV halo. Further investigation into a more comprehensive physical model to describe the emission will be the focus of future work.

## 5. Conclusions

The new observations from HAWC in the region of IC 443 reinforce the importance of continuing to study this supernova remnant. The question of whether IC 443 is a PeVatron remains open. As discussed, if protons are indeed accelerated to PeV energies within this remnant, they could produce a significant gamma-ray contribution above 20 TeV, supporting the possibility of IC 443 as a PeVatron candidate. HAWC observations estimate the maximum proton energy to be above the theoretical minimum of 65 TeV, with no evidence of a cutoff in the gamma-ray spectrum, suggesting that further observations are essential to explore the potential for acceleration to PeV energies.

While HAWC has also now detected an extended source in the region, which we called HAWC J0615+2213, with a centroid near the pulsar B0611+22, initial analyses indicate that cosmic-ray interactions with nearby gas cannot fully account for this emission. Estimates in Sect. 4, provide evidence that this extended source may represent a new TeV halo, whose detailed study will be the focus of a future publication. Observations from LHAASO could help confirm this new source. Future experiments like SWGO could enhance the detection of additional halos in regions beyond HAWC's current reach.

*Acknowledgements.* We acknowledge the support from: the US National Science Foundation (NSF); the US Department of Energy Office of High-Energy Physics; the Laboratory Directed Research and Development (LDRD) program of Los Alamos National Laboratory; Consejo Nacional de Ciencia y Tecnología (CONACYT), México, grants LNC-2023-117, 271051, 232656, 260378, 179588, 254964, 258865, 243290, 132197, A1-S-46288, A1-S-22784, CF-2023-I-645, cátedras 873, 1563, 341, 323, Red HAWC, México; DGAPA-UNAM grants IG101323, IN111716-3, IN111419, IA102019, IN106521, IN114924, IN110521, IN102223; VIEP-BUAP; PIFI 2012, 2013, PROFOCIE 2014, 2015; the University of Wisconsin Alumni Research Foundation; the Institute of Geophysics, Planetary Physics, and Signatures at Los Alamos National Laboratory; Polish Science Centre grant, 2024/53/B/ST9/02671; Coordinación de la Investigación Científica de la Universidad Michoacana; Royal Society - Newton Advanced Fellowship 180385; Gobierno de España and European Union - NextGenerationEU, grant CNS2023- 144099; The Program Management Unit for Human Resources & Institutional Development, Research and Innovation, NXPO (grant number B16F630069); Coordinación General Académica e Innovación (CGAI-UdeG), PRODEP-SEP UDG-CA-499; Institute of Cosmic Ray Research (ICRR), University of Tokyo. H.F. acknowledges support by NASA under award number 80GSFC21M0002. C.R. acknowledges support from National Research Foundation of Korea (RS-2023-00280210). We also acknowledge the significant contributions over many years of Stefan Westerhoff, Gaurang Yodh and Arnulfo Zepeda Domínguez, all deceased members of the HAWC collaboration. Thanks to Scott Delay, Luciano Díaz and Eduardo Murrieta for technical support.

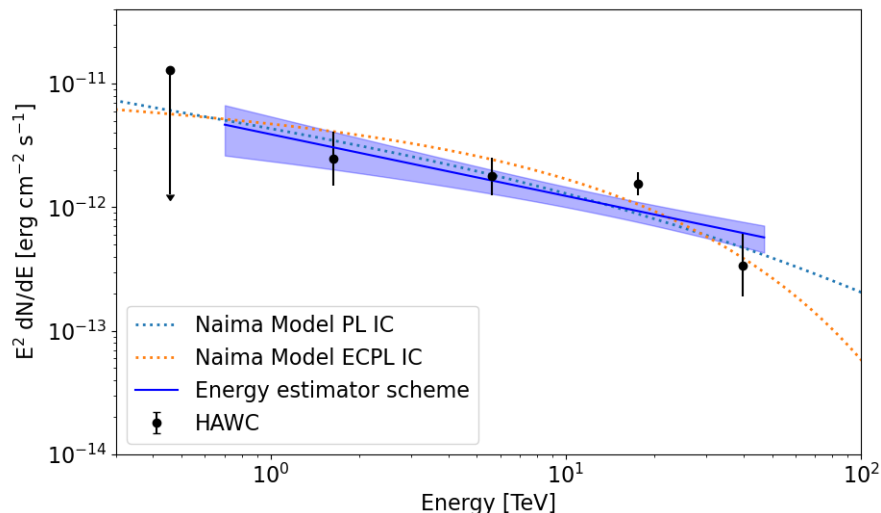


**Fig. 8.** Spectrum of the extended source. A physical model assuming only inverse Compton is tested. Both simpler power law and exponential cutoff models for the electron spectrum can describe the data. The results of the parameters are used to estimate the electron energy density. For comparison, we show the power law fit to the HAWC data using the energy estimator scheme.

## References

- Abdo, A. A., Ackermann, M., Ajello, M., et al. 2009, *ApJL*, 706, L1  
 Abdo, A. A., Ackermann, M., Ajello, M., et al. 2010, *ApJ*, 712, 459  
 Abeyssekara, A. U., Albert, A., Alfaro, R., et al. 2019, *ApJ*, 881, 134  
 Abeyssekara, A. U., Albert, A., Alfaro, R., et al. 2017, *ApJ*, 843, 39  
 Abeyssekara, A. U., Albert, A., Alfaro, R., et al. 2022, in 37th International Cosmic Ray Conference, 828  
 Abeyssekara, A. U., Albert, A., Alfaro, R., et al. 2023, *Nuclear Instruments and Methods in Physics Research Section A*, 1052, 168253  
 Abramowski, A., Aharonian, F., Benkhali, F. A., et al. 2016, *Nature*, 531, 476  
 Acciari, V. A., Aliu, E., Arlen, T., et al. 2009, *ApJL*, 698, L133  
 Ackermann, M., Ajello, M., Allafort, A., et al. 2013, *Science*, 339, 807  
 Albert, A., Alfaro, R., Alvarez, C., et al. 2024, *ApJ*, 972, 144  
 Albert, A., Alfaro, R., Alvarez, C., et al. 2021, *ApJ*, 914, 106  
 Albert, A., Alfaro, R., Alvarez, C., & HAWC Collaboration. 2020, *ApJ*, 905, 76  
 Albert, A., Alvarez, C., Avila Rojas, D., et al. 2023, *ApJ*, 954, 205  
 Albert, J., Aliu, E., Anderhub, H., et al. 2007, *ApJL*, 664, L87  
 Ambrocio-Cruz, P., Rosado, M., de la Fuente, E., Silva, R., & Blanco-Piñon, A. 2017, *MNRAS*, 472, 51  
 Atoyan, A. M., Aharonian, F. A., & Völk, H. J. 1995, *Phys. Rev. D*, 52, 3265  
 Baring, M. G., Ellison, D. C., Reynolds, S. P., Grenier, I. A., & Goret, P. 1999, *ApJ*, 513, 311  
 Bell, A. R. 2004, *MNRAS*, 353, 550  
 Bell, A. R., Schure, K. M., Reville, B., & Giacinti, G. 2013, *Monthly Notices of the Royal Astronomical Society*, 431, 415  
 Camilloni, F. & Becker, W. 2023, *AAP*, 680, A83  
 Cao, Z., Aharonian, F., An, Q., Axikegu, & (The Lhaaso Collaboration). 2024, *ApJS*, 271, 25  
 Caprioli, D., Blasi, P., Amato, E., & Vietri, M. 2009, *MNRAS*, 395, 895  
 Castelletti, G., Dubner, G., Clarke, T., & Kassim, N. E. 2011, *AAP*, 534, A21  
 Chevalier, R. A. 1999, *ApJ*, 511, 798  
 Cristofari, P., Blasi, P., & Amato, E. 2020, *Astroparticle Physics*, 123, 102492  
 Dame, T. M., Ungerechts, H., Cohen, R. S., et al. 1987, *ApJ*, 322, 706  
 Davies, J. and Lyne, A. and Seiradakis, J. 1972, *Nature*, 240, 229  
 Deller, A. T., Goss, W. M., Brisken, W. F., et al. 2019, *ApJ*, 875, 100  
 Drury, L. O. 1983, *Reports on Progress in Physics*, 46, 973  
 Dundovic, A., Evoli, C., Gaggero, D., & Grasso, D. 2021, *AAP*, 653, A18  
 Erickson, W. C. & Mahoney, M. J. 1985, *ApJ*, 290, 596  
 Evoli, C., Gaggero, D., Vittino, A., et al. 2017, *JCAP*, 2017, 015  
 Fesen, R. A. 1984, *ApJ*, 281, 658  
 Gaensler, B. M., Chatterjee, S., Slane, P. O., et al. 2006, *ApJ*, 648, 1037  
 Giacinti, G., Mitchell, A. M. W., López-Coto, R., et al. 2020, *A&A*, 636, A113  
 Green, D. A. 2019, *Journal of Astrophysics and Astronomy*, 40, 36  
 Guo, F., Li, H., Daughton, W., & Liu, Y.-H. 2014, *PRL*, 113, 155005  
 HI4PI Collaboration, Ben Bekhti, N., Flöer, L., et al. 2016, *AAP*, 594, A116  
 Lagage, P. O. & Cesarsky, C. J. 1983, *Astronomy and Astrophysics*, 118, 223  
 Lee, J.-J., Koo, B.-C., Yun, M. S., et al. 2008, *AJ*, 135, 796  
 Lee, J.-J., Koo, B.-C., Yun, M. S., et al. 2008, *The Astronomical Journal*, 135, 796  
 Li, J., Jiang, B., & Zhao, H. 2022, *ApJ*, 927, 226  
 Linden, T., Auchettl, K., Bramante, J., et al. 2017, *Phys. Rev. D*, 96, 103016  
 Olbert, C. M., Clearfield, C. R., Williams, N. E., Keohane, J. W., & Frail, D. A. 2001, *ApJ*, 554, L205  
 Petrosian, V. 2012, *Space Science Reviews*, 173, 535  
 Planck Collaboration et al. 2011, *A&A*, 536, 16  
 Rajwade, K., Seymour, A., Lorimer, D. R., et al. 2016, *MNRAS*, 462, 2518  
 Seta, M., Hasegawa, T., Dame, T. M., et al. 1998, *ApJ*, 505, 286

- Sharma, P., Ou, Z., Henry-Cadrot, C., Dubos, C., & Suomijärvi, T. 2023, JCAP, 2023, 027  
Troja, E., Bocchino, F., Miceli, M., & Reale, F. 2008, A&A, 485, 777  
Troja, E., Bocchino, F., Miceli, M., Reale, F., & Dubner, G. 2008, The Astrophysical Journal, 689, L125  
Troja, E., Bocchino, F., & Reale, F. 2006, ApJ, 649, 258  
Ustamujic, S., Orlando, S., Greco, E., et al. 2021, AAP, 649, A14  
Vianello, G., Lauer, R. J., Younk, P., et al. 2015, arXiv e-prints, arXiv:1507.08343  
Vink, J. 2022, Frascati Phys.Ser., 74, 153  
Wenger, T. V., Balsler, D. S., Anderson, L. D., & Bania, T. M. 2018, ApJ, 856, 52  
Wolf, M. 1893, AN, [3130] 131, 157  
Yamaguchi, H., Ozawa, M., Koyama, K., et al. 2009, The Astrophysical Journal, 705, L6  
Yao, J. M., Manchester, R. N., & Wang, N. 2017, ApJ, 835, 29  
Zabalza, V. 2015, in International Cosmic Ray Conference, Vol. 34, 34th International Cosmic Ray Conference (ICRC2015), 922  
Zhang, B. & Yan, H. 2011, ApJ, 726, 90  
Zhang, S., Tang, X., Zhang, X., et al. 2018, ApJ, 859, 141

- 
- <sup>1</sup> Instituto de Física, Universidad Nacional Autónoma de México, Ciudad de México, Mexico  
<sup>2</sup> Universidad Autónoma de Chiapas, Tuxtla Gutiérrez, Chiapas, México  
<sup>3</sup> Escuela de Física, Universidad de Costa Rica, San José, Costa Rica  
<sup>4</sup> Universidad Michoacana de San Nicolás de Hidalgo, Morelia, Mexico  
<sup>5</sup> Instituto de Astronomía, Universidad Nacional Autónoma de México, Ciudad de México, Mexico  
<sup>6</sup> Department of Physics, Pennsylvania State University, University Park, PA, USA  
<sup>7</sup> Department of Physics and Astronomy, Michigan State University, East Lansing, MI, USA  
<sup>8</sup> Università degli Studi di Torino, I-10125 Torino, Italy  
<sup>9</sup> Instituto Nacional de Astrofísica, Óptica y Electrónica, Puebla, Mexico  
<sup>10</sup> Institute of Nuclear Physics Polish Academy of Sciences, PL-31342 IFJ-PAN, Krakow, Poland  
<sup>11</sup> Facultad de Ciencias Físico Matemáticas, Benemérita Universidad Autónoma de Puebla, Puebla, Mexico  
<sup>12</sup> Instituto de Física Corpuscular, CSIC, Universitat de Valencia, Paterna, Valencia, Spain  
<sup>13</sup> Departamento de Física, Centro Universitario de Ciencias Exactas e Ingenierías, Universidad de Guadalajara, Guadalajara, Mexico  
<sup>14</sup> Max-Planck Institute for Nuclear Physics, 69117 Heidelberg, Germany  
<sup>15</sup> Department of Physics, University of Wisconsin-Madison, Madison, WI, USA  
<sup>16</sup> Department of Physics, Stanford University: Stanford, CA 94305–4060, USA  
<sup>17</sup> Los Alamos National Laboratory, Los Alamos, NM, USA  
<sup>18</sup> Tecnológico de Monterrey, Escuela de Ingeniería y Ciencias, Ave. Eugenio Garza Sada 2501, Monterrey, N.L., Mexico, 64849  
<sup>19</sup> Department of Physics, University of Maryland, College Park, MD, USA  
<sup>20</sup> Universidad Politécnica de Pachuca, Pachuca, Hgo, Mexico  
<sup>21</sup> Instituto de Geofísica, Universidad Nacional Autónoma de México, Ciudad de México, Mexico  
<sup>22</sup> University of Seoul, Seoul, Rep. of Korea  
<sup>23</sup> College of Science and Technology, Temple University, Philadelphia, PA, USA  
<sup>24</sup> Centro de Investigación en Computación, Instituto Politécnico Nacional, México City, México.  
<sup>25</sup> Dept of Physics and Astronomy, University of New Mexico, Albuquerque, NM, USA  
<sup>26</sup> Department of Physics, Michigan Technological University, Houghton, MI, USA  
<sup>27</sup> Universidad Autónoma del Estado de Hidalgo, Pachuca, Mexico  
<sup>28</sup> Instituto de Ciencias Nucleares, Universidad Nacional Autónoma de México, Ciudad de México, Mexico  
<sup>29</sup> Department of Physics, Sungkyunkwan University, Suwon 16419, South Korea  
<sup>30</sup> Laboratoire d'Annecy de Physique des Particules (LAPP), 9 Chemin de Bellevue, B.P. 110, F-74941 Annecy CEDEX, France  
<sup>31</sup> Department of Physics and Astronomy, University of Utah, Salt Lake City, UT, USA  
<sup>32</sup> Tsung-Dao Lee Institute & School of Physics and Astronomy, Shanghai Jiao Tong University, Shanghai, China

## Appendix A: Morphology model

### Appendix A.1: 2D Gaussian in the sphere

The general shape for the 2D gaussian is:

$$f(\mathbf{x}) = \left(\frac{180^\circ}{\pi}\right)^2 \frac{1}{2\pi \sqrt{\det \Sigma}} \exp\left(-\frac{1}{2}(\mathbf{x} - \mathbf{x}_0)^\top \cdot \Sigma^{-1} \cdot (\mathbf{x} - \mathbf{x}_0)\right) \quad (\text{A.1})$$

where :

$$\mathbf{x}_0 = (\text{RA}_0, \text{Dec}_0),$$

$$\Lambda = \begin{pmatrix} \sigma^2 & 0 \\ 0 & \sigma^2(1 - e^2) \end{pmatrix},$$

$$U = \begin{pmatrix} \cos \theta & -\sin \theta \\ \sin \theta & \cos \theta \end{pmatrix},$$

$$\Sigma = U \Lambda U^\top$$

For a symmetric gaussian,  $e = 0$  and  $\theta = 0$ .

## Appendix B: Comparison with LHAASO measurements

The LHAASO collaboration presented their catalog results in Cao et al. (2024). For the catalog search, in the region of IC 443 they found an extended sources, modeled with a 2D Gaussian function for the morphology, and a simple power-law function for the spectrum. The energy range where they significantly detect the source is between 1 TeV to 25 TeV. Using the same model, we refit the region of IC 443 using the  $f_{\text{hit}}$  scheme to compare results. One thing to consider is that in the LHAASO catalog, the galactic diffuse emission model is based on the Planck maps of dust optical depth (Planck Collaboration et al. 2011). Table B.1 and Fig. B.1 shows the results, which are consistent within uncertainties.

**Table B.1.** Results of the comparison between HAWC and LHAASO in the region of IC 443 using the same model.

Parameter	LHAASO	HAWC
R.A [deg]	94.35±0.18	94.04±0.12
Dec. [deg]	22.57±0.18	22.44±0.12
$\sigma$ [deg]	0.59±0.08	0.72±0.10
$\Phi_0$	1.95±0.27	1.54 <sup>+0.34</sup> <sub>-0.28</sub>
$\alpha$	-2.92±0.14	-2.65±0.07
GDE*	—	4.0±0.9

**Notes.** Uncertainties are statistical while the second set are systematic.  $\Phi_0$  is in units of  $10^{-13} \text{ TeV}^{-1} \text{ cm}^{-2} \text{ s}^{-1}$  and it is at a pivot of 3 TeV. \*Scale factor is unitless.

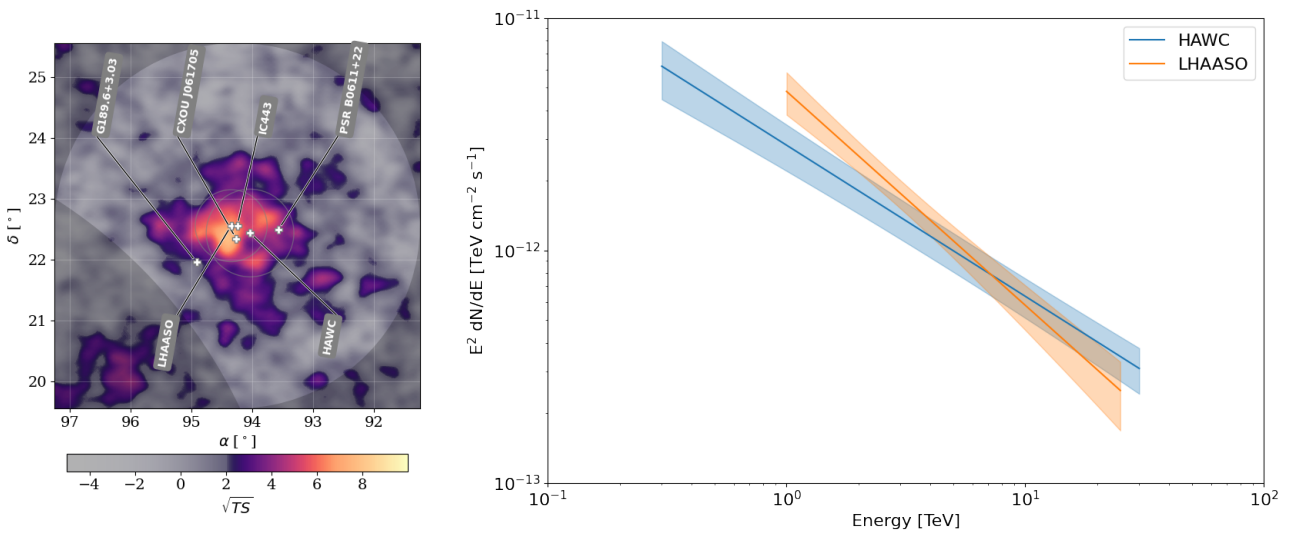


**Fig. B.1.** Left: Sky map with the positions measured by LHAASO and HAWC using only a 2D Gaussian morphology. Circles are the  $1\sigma$  of the Gaussian function. Right: SED of the extended source. Fluxes are consistent within uncertainties.

### Appendix C: Parameter results of the inverse Compton modeling of the extended source

We used Naima for the modeling. The electron spectra used when fitting the gamma-ray flux of the extended source are a simple power law and a power law with exponential cut off. For the inverse Compton model, we used the default photon fields that exist in Naima, which include CMB, near-infrared and far-infrared. The temperatures of 2.72 K, 30 K, and 3000 K, and energy densities of 0.261, 0.5, and 1 eV cm<sup>-3</sup> are used respectively for each field (Zabalza 2015). The results of these models are:

- Simple power law: Normalization:  $(5.3_{-2.5}^{+3.9}) \times 10^{47}$  erg<sup>-1</sup>; index: 3.4±0.2.
- Power law with exponential cutoff: Normalization:  $(1.3_{-1.0}^{+1.7}) \times 10^{47}$  erg<sup>-1</sup>; index: 2.9<sup>+0.4</sup><sub>-0.7</sub>; energy cutoff: 67<sup>+241</sup><sub>-44</sub> TeV.